Nano Express

PAPER • **OPEN ACCESS**

Photodetection in single-crystal 3D $MAPbI_3$ and quasi-2D $(PEA)_2(MA)Pb_2I_7$ perovskites

To cite this article: Adolfo Mazzotti *et al* 2026 *Nano Ex.* **7** 035010

NANO EXPRESS

OPEN ACCESS

RECEIVED
25 June 2026

REVISED
31 July 2026

ACCEPTED FOR PUBLICATION
12 August 2026

PUBLISHED
19 August 2026

PAPER

Photodetection in single-crystal 3D $MAPbI_3$ and quasi-2D $(PEA)_2(MA)Pb_2I_7$ perovskites

Adolfo Mazzotti[1,3], Selene Matta[2], Ofelia Durante[1], Valeria Demontis[2], Sebastiano De Stefano[1], Andrea Sessa[1], Francesco De Chiara[1], Daniela Marongiu[2], Michele Saba[2], Giovanni Bongiovanni[2], Nadia Martucciello[3] and Antonio Di Bartolomeo[1,*]

[1] Department of Physics "E.R. Caianiello", University of Salerno, Via Giovanni Paolo II 132, Fisciano, SA 84084, Italy
[2] Department of Physics, University of Cagliari, Monserrato, CA 09042, Italy
[3] CNR-SPIN, Via Giovanni Paolo II 132, Fisciano, SA 84084, Italy
[*] Author to whom any correspondence should be addressed.

E-mail: adibartolomeo@unisa.it

Keywords: perovskites, photodetector, quasi-2D $(PEA)_2(MA)Pb_2I_7$, $MAPbI_3$, organic spacer layers, low-noise photodetection

Supplementary material for this article is available online

Abstract

Hybrid organic–inorganic perovskites are emerging as key materials for next-generation photodetectors, where the compositional and structural tunability and exceptional optoelectronic properties provide a powerful strategy to tune the microscopic mechanisms governing the photoresponse. Here, 3D $MAPbI_3$ and quasi-2D $(PEA)_2(MA)Pb_2I_7$ single-crystal photodetectors are comparatively investigated under dark and illuminated conditions. The devices employ two lateral Ag-paste contacts and therefore operate as photoconductors, in which illumination increases the crystal conductivity through the generation of mobile charge carriers under an applied bias. Both devices exhibit a nearly ohmic behavior in the dark and under illumination. The photocurrent increases almost linearly with the incident optical power, with a power-law exponentia of $\alpha \approx 0.9$ for both crystals. The 3D perovskite shows higher conductivity, with a dark current of 10^{-10} A at $V_{bias} = 1$ V, whereas the quasi-2D device exhibits a strongly suppressed dark current of 10^{-12} A under the same bias condition. Prompt and reversible photocurrent switching is observed in both devices within the temporal resolution of the experimental setup; however, the 3D crystal also displays an additional slow current rise, suggesting the activation of a secondary light-induced process. Spectral measurements further reveal a widened bandgap in the quasi-2D perovskite, consistent with its layered structure. Overall, this comparative study highlights the key role of dimensionality and organic-cation engineering in balancing efficient photogeneration, dark-current suppression, and low-noise photodetection.

1. Introduction

Semiconducting materials have long been at the core of optoelectronic technologies, from conventional p–n junction diodes to advanced light-emitting, photovoltaic, and photodetection devices [1, 2]. In recent years, the development of low-dimensional semiconductors has opened new routes to engineer light–matter interaction at the nanoscale. In systems such as nanoparticles [3, 4], nanowires [5, 6], and atomically thin two-dimensional materials [7–10], quantum confinement along one or more spatial directions can strongly modify the electronic structure, leading to bandgap widening and enhanced optical absorption. Within this broad scenario, metal halide perovskites represent a particularly promising class of semiconductors, as they combine strong light absorption, tunable bandgaps, low-temperature processability, and mixed electronic–ionic dynamics [11–13]. Hybrid organic–inorganic metal halide

perovskites are generally described by the ABX_3 structure, where A is an organic or inorganic monovalent cation, B is a metal cation, and X is a halide anion. In their three-dimensional phase, the corner-sharing BX_6 octahedra form a continuous inorganic framework that enables efficient charge transport and strong optical absorption. Their remarkable optoelectronic properties are exemplified by long carrier diffusion lengths and excellent light-harvesting capability in $MAPbI_3$-based systems [14, 15]. These features have enabled a broad range of applications. For instance, high-performance perovskite solar cells based on $MAPbI_3$ have been demonstrated through improved film-growth strategies [14], while solution-grown $MAPbI_3$ula>single-crystals were reported to exhibit electron and hole diffusion lengths exceeding 175 μm under one-sun illumination [15]. In addition, three-dimensional metal-halide perovskites have been successfully employed in light-emitting diodes with bright and tunable electroluminescence [16], in highly sensitive photodetectors with detectivities approaching 10^{14} Jones [17], and in direct x-ray detectors owing to the strong x-ray absorption associated with Pb and I atoms [18]. Besides, the continued study of these perovskite materials remains essential, as new device-engineering strategies are constantly being developed to improve their optoelectronic performance, stability, and charge-collection efficiency. For example, MoO_3/metal/MoO_3 multilayer transparent electrodes have been investigated to balance optical transmittance and electrical conductivity in semitransparent $MAPbI_3$ solar cells, while TiO_2/SnO_2 bilayer electron-transport layers have been proposed to enhance electron extraction and suppress interfacial recombination in such devices [19, 20].

At the same time, ion migration and defect-mediated transport in 3D perovskites can give rise to complex light-induced phenomena, which have been exploited for reconfigurable memory and neuromorphic functionalities, although long-term stability remains a major challenge [21].

A powerful strategy to overcome part of these limitations consists in engineered perovskites, with bulky organic spacer cations introduced into the lattice to separate the inorganic slabs and form layered quasi-2D structures. These insulating organic layers not only improve environmental robustness, but also generate natural quantum-well architectures, enhance quantum and dielectric confinement, and preserve efficient in-plane charge transport [22, 23]. High-field magneto-absorption measurements on phase-pure PEA-based perovskites revealed tightly bound excitons, with binding energies of approximately 400 meV [24]. Centimeter-scale lateral heterostructures combining $(PEA)_2PbI_4$ and $(PEA)_2MAPb_2I_7$ have also been demonstrated for narrow and wavelength-selective dual-band photodetection [25]. Moreover, solid-state NMR measurements showed that the rigid aromatic PEA spacer restricts the reorientational motion of the MA cations more effectively than flexible alkyl spacers and prevents significant structural changes during cooling [26]. As a result, quasi-2D perovskites offer a unique platform to investigate how organic-layer engineering reshapes photogeneration, charge transport, ionic motion, and noise mechanisms in photodetector devices.

In this work, photodetecting devices based on two different perovskite phases, namely 3D $MAPbI_3$ and quasi-2D $(PEA)_2(MA)Pb_2I_7$, are fabricated and comparatively investigated. In the present device configuration, both Ag-paste electrodes directly contact the same perovskite crystal in a lateral two-terminal geometry. Photon absorption generates mobile electron–hole pairs that increase electrical conductance under an externally applied bias. The nearly linear and approximately symmetric current–voltage characteristics observed in both devices are consistent with this operating mechanism. Their optoelectronic response is analyzed as a function of both incident optical power and excitation wavelength, allowing the role of structural dimensionality in light detection to be assessed. The presence of organic spacer layers in the quasi-2D phase strongly modifies charge transport and interfacial dynamics, affecting dark current, noise level, and overall photodetector performance. This comparison highlights how the continuous inorganic framework of the 3D perovskite and the layered quantum-well-like architecture of the quasi-2D structure give rise to distinct photoresponse mechanisms, providing insight into the design of low-noise perovskite-based photodetectors.

2. Materials and methods

2.1. Fabrication process and device morphology

Perovskite single-crystals, namely the quasi-2D $(PEA)_2(MA)Pb_2I_7$ and 3D $MAPbI_3$ phases, were grown using a space-confined technique [27]. The precursor solution was prepared with methylammonium iodide (MAI, 99.99%), ammonium chloride (NH_4Cl, $\geqslant$99.5%), lead iodide (PbI_2, 99.999%), phenethylammonium iodide (PEAI, 98.00%) and γ-butyrolactone (GBL, 99+%), following the procedure reported in previous works [27, 28]. Afterwards, two quartz substrates of different dimensions (2.5 $\times$ 2.5 cm^2 and 1.5 $\times$ 1.5 cm^2) were cleaned and stacked. This size mismatch is intended to improve deposition reproducibility by facilitating assembly and promoting effective edge sealing, thereby enabling

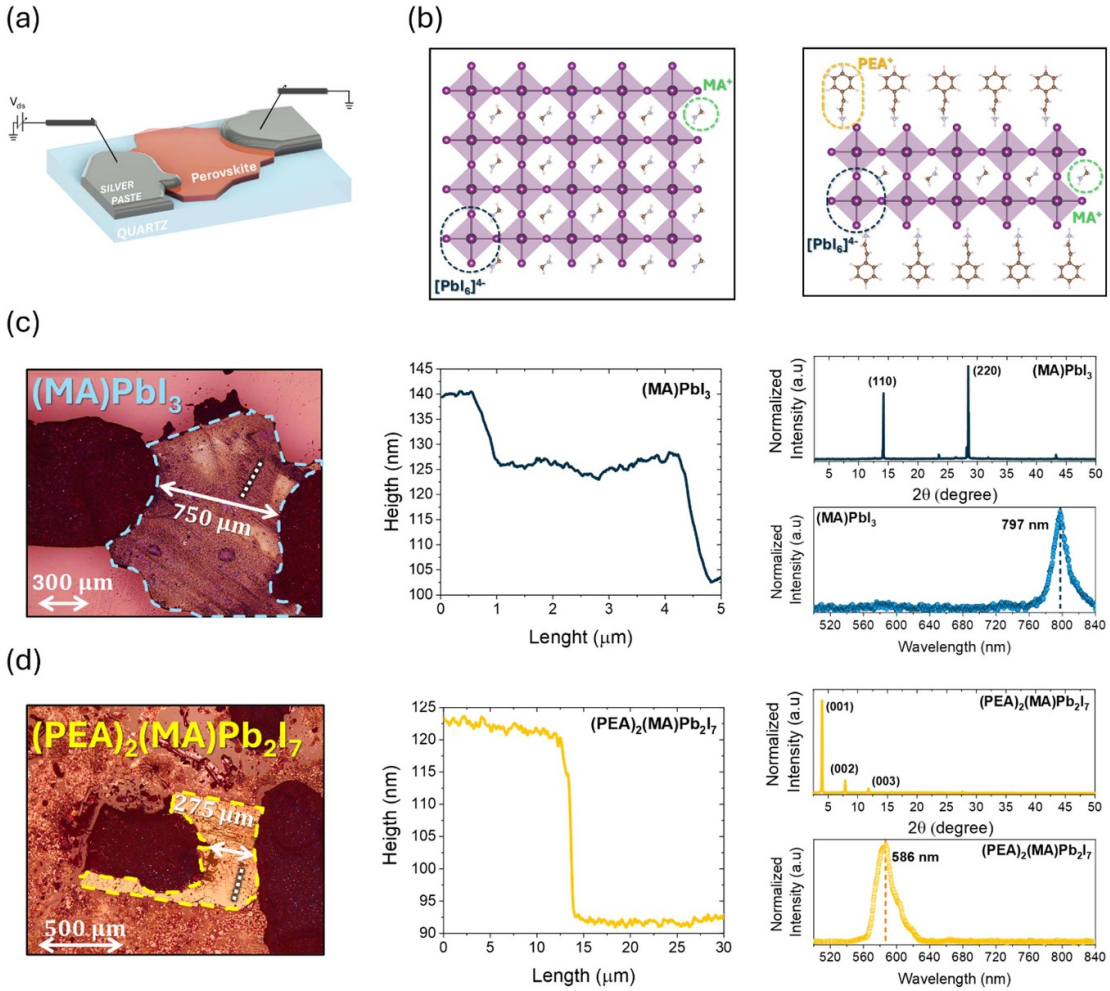

Figure 1. Crystal structures and morphology. (a) Schematic representation of the two-terminal perovskite device. (b) Crystal structure of 3D $MAPbI_3$ (left panel) and of the quasi-2D $(PEA)_2(MA)Pb_2I_7$ (right panel), the dashed blue circle highlights the $[PbI_6]^{4-}$ octahedron, the green one marks the $(MA)^+$ cation and the yellow one the $(PEA)^+$ cation. (c) Optical image of the 3D perovskite device (left panel), the crystal area is marked by a dashed blue contour; AFM height profile of the crystal (central panel) along the path shown as a white dashed line in the left panel; XRD pattern (top) and photoluminescence (bottom) of the 3D crystal (right panel). (d) Optical image of the quasi-2D perovskite device (left panel), the crystal area is highlighted by a dashed yellow contour; AFM height profile of the crystal (central panel) along the path shown as a white dashed line in the left panel; XRD pattern (top) and photoluminescence (bottom) of the quasi-2D crystal (right panel).

more controlled solvent evaporation and crystallization kinetics. A 10 μL droplet of the precursor solution was then deposited along the edge of the upper substrate, allowing capillary-driven infiltration into the confined space between the two substrates. The samples were thermally cycled between 373.15 K and 413.15 K at a rate of 4 K h^{-1}, with 10 h holds at both temperatures. This thermal protocol was designed to promote the formation of both quasi-2D and 3D perovskite crystals. Finally, the samples were vacuum-dried, and the two quartz substrates were carefully separated, resulting in individual quartz-supported perovskite crystals containing either quasi-2D or 3D phases. To perform electrical transport measurements, two droplets of silver paste were deposited on selected regions of each crystal, forming metallic contact pads suitable for probing. This approach enables a stable electrical connection to the fragile perovskite crystal while minimizing mechanical damage and reducing the contact resistance. A schematic representation of the resulting two-terminal device is shown in figure 1(a), where a single perovskite crystal bridges two silver-paste electrodes on a quartz substrate.

The crystal structures of the two perovskite phases are shown in figure 1(b). The 3D $(MA)PbI_3$ perovskite, reported in the left panel, consists of a continuous three-dimensional network of corner-sharing PbI_6 octahedra, with MA+ cations occupying the cavities of the inorganic framework. This extended connectivity allows charge transport in all crystallographic directions and gives rise to the typical 3D perovskite electronic structure. In contrast, $(PEA)_2MAPb_2I_7$, reported in the right panel, is a layered perovskite, obtained by slicing the 3D framework along the {100} planes. In this structure, the inorganic component consists of two layers of corner-sharing PbI_6 octahedra separated by bulky

phenethylammonium (PEA^+) spacer cations, while methylammonium (MA^+) remains confined within the inorganic slabs. Therefore, the main structural difference is the reduced dimensionality: $(MA)PbI_3$ forms a fully connected 3D Pb–I network, whereas $(PEA)_2MAPb_2I_7$ consists of quasi-2D inorganic quantum wells isolated by organic PEA^+ layers. The left panel of figure 1(c) shows the optical image of the 3D $MAPbI_3$, highlighted by a dashed blue contour. The irregular areas of both the quasi-2D and 3D crystals were determined using the software ImageJ after spatial calibration with the scale bar. The contour of each crystal was independently traced ten times. The reported active area corresponds to the mean of the repeated measurements, while their standard deviation was used as the uncertainty associated with contour selection. The minimum electrode spacing, L_{min}, was measured as the shortest edge-to-edge distance between the two Ag-paste electrodes on the same calibrated optical images. The estimated area of the $(MA)PbI_3$ crystal is $A_{3D} = (0.948 \pm 0.005)$ mm^2, while $L_{min} = 750$ μm. The morphology of the crystal was investigated by atomic force microscopy (AFM). The corresponding 3D perovskite AFM profile along the path shown as a white dashed line in the optical image, reported in the central panel of figure 1(c), reveals the presence of well-defined terraces, indicating a stepped growth morphology. The surface appears slightly irregular and is characterized by terrace heights of approximately 15 nm and 25 nm. The right panel of figure 1(c) shows the XRD pattern (top) and the normalized steady-state photoluminescence spectrum (bottom) of the 3D crystal. The XRD pattern is dominated by two sharp reflections at 14° and 28°, which are attributed to the tetragonal phase of $MAPbI_3$. These reflections can be indexed as the (110), (220), … (hk0) planes, indicating that they arise from a set of parallel lattice planes. This suggests a preferential orientation of the crystals, with dominant growth along the (hk0) direction and the c-axis lying parallel to the substrate surface. The narrow reflections indicate the high crystallinity of the as-grown crystals and are consistent with their single-crystalline nature. The photoluminescence spectrum exhibits a dominant emission band centered at 797 nm, corresponding to a photon energy of approximately 1.56 eV. This value is consistent with the near-band-edge emission commonly reported for three-dimensional $(MA)PbI_3$ and is remarkably close to the 795 nm emission assigned to the direct-gap transition in bulk $(MA)PbI_3$ single-crystals [29]. The presence of a single dominant band indicates that the optical response is mainly governed by radiative recombination close to the band edge, while no intense broad deep-subgap emission is observed within the investigated spectral range [30].

The optical image of the quasi-2D $(PEA)_2(MA)Pb_2I_7$ is reported in the left panel of figure 1(d), highlighted by a dashed yellow contour, with an estimated area of $A_{2D} = (0.284 \pm 0.002)$ mm^2 and $L_{min} = 275$ μm. The AFM profile, shown in the central panel, also reveals a terraced morphology, but with a more regular surface characterized by terraces with an average height of approximately 33 nm. The observation of terraces in both samples is consistent with a layer-by-layer growth mechanism, suggesting a relatively controlled crystallization process and a good degree of structural order within the crystals. The right panel shows the XRD pattern (top) and the normalized steady-state photoluminescence spectrum (bottom) of the $(PEA)_2(MA)Pb_2I_7$. Also, for the quasi-2D phase, the diffraction pattern is dominated by sharp reflections, indicating the high crystallinity of the as-grown perovskite crystals and supporting their single-crystalline nature. In particular, the intense low-angle reflections belonging to the (00l) family reveal a pronounced preferential orientation, with the inorganic perovskite layers predominantly aligned parallel to the substrate surface. The photoluminescence spectrum of the layered quasi-2D perovskite exhibits a dominant emission band centered at 586 nm, corresponding to an energy of approximately 2.12 eV. This value is consistent with the near-band-edge emission commonly reported for the ($n = 2$) member of the PEA-based Ruddlesden–Popper perovskite family, whose room-temperature photoluminescence is generally observed in the 575–590 nm spectral range [31, 32].

2.2. Experimental setup

The perovskite diffraction patterns were collected using a powder diffractometer (D8 ADVANCE, Bruker) employing a Cu Kα radiation (40 kV/40 mA) and a Goebel Mirror with UBC collimator 0.3 mm. The sample was placed on a UMC stage (motorized XYZ) and the patterns were recorded with the Detector LYNXEYE XE-T (1D continuous mode) with 0.03 deg/step and 0.5 s/step. Electrical measurements were conducted in a two-probe configuration using a Keithley 4200-SCS semiconductor characterization system coupled to a Lakeshore TTPX cryogenic probe station. Photoresponse measurements were carried out under both supercontinuum light and monochromatic illumination. The light source was a supercontinuum laser (SuperK Compact, NKT Photonics; 450–2400 nm spectral range), either used directly for broadband illumination or coupled to a monochromator for wavelength-resolved measurements. All measurements were conducted in air at ambient pressure and temperature.

3. Results and discussion

3.1. Photoresponse to increasing power

Figure 2(a) shows the current–voltage, *IV*, characteristics of the 3D perovskite crystal measured by sweeping the bias voltage between −1 V and +1 V in both sweep directions, under dark conditions and under supercontinuum laser illumination. The maximum laser power is $P_{opt} = 16.5$ mW distributed over a laser spot area of $S = 1$ mm^2. The incident laser power is $P_{inc} = (P_{opt} \cdot A_{act})/S$, where A_{act} is the effective photoactive area. In the present analysis, A_{act} was taken as the entire crystal area, since photocarriers generated throughout the crystal, including in peripheral regions outside the shortest path between the electrodes, may be collected at the contacts and contribute to the measured photocurrent. P_{inc} was progressively increased from 1.6 mW to 14.0 mW, while the measurements were performed at ambient temperature and pressure. The device exhibits a pronounced photoresponse, with the current systematically increasing upon illumination, indicating an enhancement of the crystal conductivity. In particular, at $V_{bias} = 1$ V, the current corresponds to 0.3 nA under dark conditions and reaches approximately 25 nA under the highest incident laser power. This behavior is consistent with a direct photoconductive process, where light absorption promotes the generation of electron–hole pairs, thereby increasing the density of mobile charge carriers contributing to transport. Independently of the illumination conditions, the *IV* curves display an approximately linear behavior and no hysteresis between the forward and reverse sweeps. Indeed, the hysteresis can be quantitatively assessed using the hysteresis index $H = (I_{forward} - I_{reverse})/I_{forward}$ at $V = 0.5$ V. Under the maximum laser power, where the largest difference between the forward and reverse voltage sweeps is observed, $H = 0.1$, confirming the limited hysteresis. This suggests an ohmic electrical response, with relatively stable contacts and limited slow charge-trapping effects within the considered voltage range [33, 34]. The inset in figure 2(a) shows the conductance, extracted from a linear fit of the *IV* curves, as a function of the incident laser power. The maximum conductance value is $G = 22.4$ nS, for $P_{inc} = 14.0$ mW.

Time-resolved photocurrent measurements were performed to investigate the photocarrier dynamics of the 3D $MAPbI_3$ crystal. Figure 2(b) reports the current transient measured at $V_{bias} = 1$ V under 10 s supercontinuum laser pulses with increasing incident power, at ambient pressure and temperature. Consistently with the *IV* curves, the photocurrent increases with laser power. The device displays a fast and reversible response: the current rapidly rises when the laser is turned on and returns to the dark baseline immediately after the illumination is removed, with no evident persistent photocurrent. Since the temporal resolution of the measurement setup is 10 ms, the rise and fall transients are not temporally resolved. Therefore, no quantitative response time is extracted from the present measurements. This behavior indicates that the dominant contribution to the photoresponse arises from direct photogeneration of mobile charge carriers, followed by their efficient extraction or recombination once the illumination is removed. At higher incident powers, above approximately 6 mW, the rising edge of the photocurrent shows a two-step dynamic. After an initial fast increase, a slower current rise develops and reaches a quasi-saturated value within about 2 s. This secondary component suggests the activation of an additional light-induced process at high photon flux. Notably, such slow dynamic is only observed during the rising part of the optical pulse, whereas the current rapidly returns to the dark baseline when the laser is switched off, with no evident delayed decay or persistent photocurrent within the experimental time scale. In general, slow photoinduced current variations in perovskite devices may originate from different and potentially concurrent processes, including carrier trapping and detrapping, changes in interfacial charge accumulation, band bending, and redistribution of mobile ionic defects. Among these possible mechanisms, the behavior observed here may be interpreted in terms of a slow reconfiguration of the mixed ionic–electronic system, determining an inductive-like photoresponse [35]. This transient modification of the electrostatic landscape may promote the redistribution of mobile ionic defects, such as iodide vacancies, which respond on a much slower time scale than electronic carriers [36–38]. As the ionic configuration evolves during illumination, it can progressively reduce the effective resistance of the device and/or improve carrier extraction by partially screening unfavorable internal fields, reducing interfacial barriers, or suppressing recombination losses [39]. At lower excitation powers, light-induced thermal effects may be insufficient to drive significant ion redistribution, even under prolonged illumination. At higher powers, however, thermally enhanced ionic motion may reduce carrier mobility and lead to a slower response. At both low and high excitation powers, the photocurrent reaches a saturation regime, reflecting a balance between photogeneration and recombination processes. Once this steady state is established, extending the illumination does not further increase the density of photogenerated carriers. The absence of a corresponding slow decay after switching the laser off suggests that once illumination is removed, the photocarrier population collapses rapidly, so the photocurrent vanishes even if the ionic configuration has not immediately relaxed back to its initial state [37, 40].

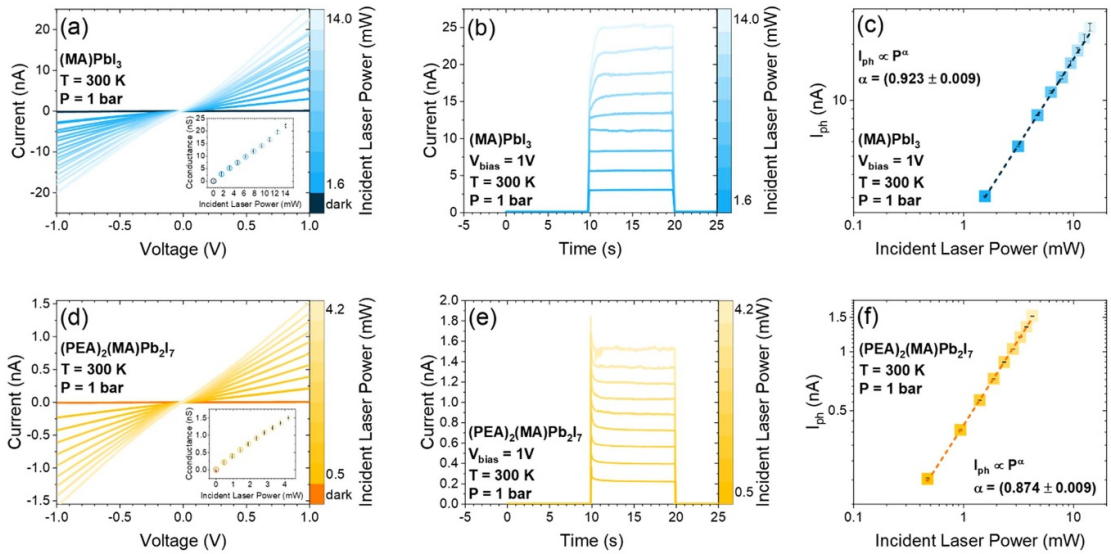

Figure 2. Electrical characterization under illumination. (a) IV characteristics of the 3D perovskite crystal measured by sweeping the bias voltage between −1 V and +1 V in both sweep directions, under dark conditions and under increasing supercontinuum laser power. The inset shows conductance as a function of the incident laser power. (b) Current versus time measured at $V_{bias} = 1$ V under 10 s supercontinuum laser pulses with increasing incident power. (c) Extracted photocurrent as a function of the incident laser power on a double-logarithmic plot with linear fit of the data (dashed blue line). (d) IV characteristics of the quasi-2D perovskite crystal measured by sweeping the bias voltage between −1 V and +1 V in both sweep directions, under dark conditions and under increasing supercontinuum laser power. The inset shows conductance as a function of the incident laser power. (e) Current versus time measured at $V_{bias} = 1$ V under 10 s supercontinuum laser pulses with increasing incident power. (f) Extracted photocurrent as a function of the incident laser power on a double-logarithmic plot with linear fit of the data (dashed orange line). All measurements were conducted at ambient temperature and pressure.

Figure 2(c) reports the photocurrent extracted from the time-resolved measurements as a function of the incident laser power, plotted on a double-logarithmic scale at $V_{bias} = 1$ V, under ambient pressure and temperature. The data follow a power-law dependence, $I_{ph} \propto P_{inc}^{\alpha}$, as evidenced by the linear fit in the log–log representation. The extracted exponent, $\alpha = (0.923 \pm 0.009)$, is close to unity, indicating an almost linear increase of the photocurrent with the incident optical power. This near-unity exponent suggests that the photoresponse of the 3D $MAPbI_3$ crystal is mainly governed by direct photogeneration of electron–hole pairs and efficient carrier collection [41]. In an ideal photoconductive regime, a linear dependence of I_{ph} on P_{inc} is expected, since the number of generated carriers scales proportionally with the photon flux. The slight deviation from $\alpha = 1$ points to a weak sublinear behavior, which can be ascribed to non-ideal processes such as trap-assisted recombination, partial filling of defect states, or the onset of carrier-density-dependent recombination at higher illumination levels [41]. Nevertheless, the value of α close to unity confirms that the device preserves a highly linear and reproducible photodetection response over the investigated power range.

The same measurements were conducted on the quasi-2D $(PEA)_2(MA)Pb_2I_7$ device to highlight the effect of the bulky organic PEA spacer cations on electrical transport. Figure 2(d) shows the *IV* curves measured for the quasi-2D perovskite under dark conditions and under supercontinuum laser illumination with incident power increasing from 0.5 mW to 4.2 mW, at ambient temperature and pressure. The laser power density was kept the same as in the measurements performed on the 3D $MAPbI_3$ device; however, the smaller illuminated area, $A_{2D} = 0.284$ mm^2, of the quasi-2D crystal resulted in a lower incident power. As already observed, the current increases progressively with the incident laser power, confirming the photoactive behavior of the quasi-2D crystal. The *IV* curves are nearly linear and symmetric with respect to the bias polarity, suggesting an ohmic photoconductive response in the investigated voltage range, without rectification or hysteresis. For $V_{bias} = 1$ V, the current corresponds to 0.005 nA under dark conditions and reaches approximately 1.5 nA under maximum power. Both under dark and illumination the current is significantly lower than that observed in the 3D $MAPbI_3$ crystal under comparable conditions. This reduced conductivity can be attributed to the layered nature of the quasi-2D perovskite, where the PEA organic spacers limit charge transport across the inorganic framework and enhance carrier confinement. Specifically, the inset in figure 2(d) shows how conductance, extracted from a linear fit of the *IV* curves, increases as a function of the incident laser power. The maximum conductance value is $G = 1.5$ nS, for $P_{inc} = 4.2$ mW.

Figure 2(e) shows the current as a function of time measured at $V_{bias} = 1$ V under 10 s supercontinuum laser pulses, with incident power increasing from 0.5 mW to 4.2 mW, at ambient temperature and pressure. As expected from the *IV* curves, the photocurrent increases progressively with the incident laser power. Also in this case, the photocurrent switching occurs within the 10 ms temporal resolution of the measurement setup. Therefore, the rise and fall times cannot be quantitatively determined from the present data. In contrast to the 3D $MAPbI_3$ crystal, no slow process is observed during the optical pulse. The current rapidly reaches a stable plateau after the laser is switched on, indicating that the response is mainly governed by direct photogeneration and fast carrier collection [41]. The sharp spikes observed at the switching edges of the optical pulse may be attributed to a capacitive-like response [35]. Such switching transients may arise from different fast processes, including charge trapping and release, interfacial charge redistribution, and charging or discharging of the device capacitance. In the present device, capacitive contributions associated with the contacts and internal interfaces may play a relevant role. A possible explanation is that the sudden generation or removal of photocarriers mainly induces a rapid charging or discharging of interfacial regions, rather than activating a slow ionic rearrangement. Charge accumulation may occur at the metal/perovskite contacts and, in the layered quasi-2D structure, possibly also at the interfaces between the conductive inorganic slabs and the more insulating PEA spacer layers. When the laser is switched on, these interfacial capacitive regions can charge rapidly, producing a transient current spike superimposed on the photocurrent. Once this charge redistribution is completed, the spike disappears and only the steady photoconductive current remains. Conversely, when the laser is switched off, the accumulated charge can be rapidly released, giving rise to a corresponding spike during the falling edge of the pulse. The absence of the slow rising component observed in the 3D crystal suggests that extended ionic redistribution is less effective, or at least not dominant, in the quasi-2D perovskite within the investigated time scale. This difference may be related to the presence of the PEA spacer layers, which interrupt the continuous 3D inorganic framework and can confine both electronic and ionic motion. As a result, the transient response of the quasi-2D device appears to be dominated by fast capacitive charging and discharging processes, while the inductive-like slow response observed in the 3D $MAPbI_3$ crystal is strongly reduced.

Figure 2(f) shows the photocurrent of the quasi-2D $(PEA)_2(MA)Pb_2I_7$ device as a function of the incident laser power. The photocurrent values were extracted from the steady-state plateau of the time-resolved measurements, after the initial capacitive transient. The data follow a power-law dependence over the investigated power range. The linear fit in the log–log representation gives an exponent $\alpha = (0.874 \pm 0.009)$, indicating a slightly sublinear increase of the photocurrent with incident optical power. This behavior confirms that the photocurrent is mainly governed by light-induced generation of charge carriers. However, the deviation from the ideal linear case, $\alpha = 1$, suggests that non-ideal recombination and transport processes also contribute to the photoresponse. In the quasi-2D perovskite, such sublinear behavior may be related to the reduced charge transport efficiency. Compared with the 3D $MAPbI_3$ crystal, the lower value of α indicates a slightly stronger departure from ideal photoconductive behavior, consistent with the more confined electronic structure of the quasi-2D material. Nevertheless, the monotonic power-law trend demonstrates a reproducible and well-defined photoresponse of the quasi-2D crystal under illumination.

The photodetection performance of the devices can be evaluated in terms of responsivity ($R = I_{ph}/P_{inc}$), noise equivalent power (NEP), specific detectivity (D^*), and photocurrent-to-dark-current ratio (I_{ph}/I_{dark}). Assuming a theoretical shot-noise-limited regime, the noise current was estimated as $i_{n,shot} = \sqrt{2qI_{dark}}$, leading to $\mathrm{NEP}_{shot} = \frac{i_{n,shot}}{R} = \sqrt{2qI_{dark}}/R$. The specific detectivity was calculated as $D^*_{shot} = \frac{\sqrt{A}}{\mathrm{NEP}_{shot}} = \left(R\sqrt{A}\right)/i_{n,shot}$, where A is the active area of the device [42]. The shot-noise-limited formulation is commonly adopted as a theoretical benchmark to compare photodetector performance through the combined effects of responsivity and dark current. Importantly, direct noise measurements performed on high-quality and single-crystalline perovskite photodetectors have shown that the experimental noise can approach the theoretical shot-noise limit, supporting its use as a physically meaningful best-case [17, 43, 44]. Nevertheless, these quantities represent theoretical best-case estimates rather than experimentally measured frequency-dependent figures of merit. In particular, the shot-noise approximation neglects additional contributions such as Johnson-Nyquist noise, generation-recombination noise, contact-related fluctuations, and low-frequency $1/f$ noise. The latter is frequently associated with slow carrier trapping and detrapping processes and with defect- and interface-related fluctuations in perovskite devices [45, 46]. If $1/f$ or other additional noise contributions are significant, the actual noise-current spectral density $i_n(f)$ would exceed $i_{n,shot}$, especially at low frequencies. Consequently, the experimental $\mathrm{NEP}(f) = i_n(f)/R$ would be higher and $D^*(f) = R\sqrt{A}/i_n(f)$ would

Table 1. Photodetection performance and theoretical shot-noise-limited estimates.

Parameter ($V_{bias} = 1$ V)	$MAPbI_3$	$(PEA)_2(MA)Pb_2I_7$
I_{ph} (nA)	25	1.5
I_{dark} (nA)	0.3	0.005
R (μ A W^{-1})	1.76	0.35
NEP_{shot} (W/$\sqrt{Hz}$)	5.58×10^{-9}	3.59×10^{-9}
D^*_{shot} (Jones)	1.75×10^7	1.48×10^7
I_{ph}/I_{dark}	83.3	300

be lower than the shot-noise-limited estimates reported here. All these parameters are summarized in table 1.

The difference in photoactive area between the two devices directly affects the absolute photocurrent, since a larger illuminated crystal area can generate a larger total number of photocarriers. Therefore, I_{ph} should not be considered alone for a direct comparison of the intrinsic photoresponse of the two materials. A more meaningful comparison is provided by the responsivity, in which the photocurrent is normalized by the incident optical power calculated from the corresponding active area, and by the specific detectivity, which additionally includes normalization by the square root of the device area. Nevertheless, residual differences related to electrode spacing, contact geometry, carrier-collection efficiency, and noise mechanisms may still affect these figures of merit.

The responsivity and specific detectivity obtained in the present devices are lower than the highest values reported for optimized perovskite photodetectors in the literature [47, 48]. This difference is mainly related to the deliberately simple device architecture employed here, consisting of two lateral Ag-paste contacts without an engineered junction, spaced interdigitated electrodes or substantially higher applied fields. Such a configuration was chosen primarily to enable a direct and consistent comparison between the intrinsic photoconductive behavior of the 3D $MAPbI_3$ and quasi-2D $(PEA)_2(MA)Pb_2I_7$ crystals, rather than to maximize the absolute device performance. Further optimization could be achieved through several strategies, including the use of asymmetric electrodes with different work functions, and the incorporation of hole- and electron-transport or blocking layers. These approaches can promote more efficient carrier separation and selective extraction, enhance rectification and responsivity, and suppress dark-current injection and recombination losses, ultimately improving the specific detectivity [49, 50]. Although the 3D crystal exhibits a higher responsivity and a comparable D^*_{shot}, the quasi-2D perovskite shows a much lower dark current, reduced shot-noise level, lower NEP_{shot}, and higher I_{ph}/I_{dark} ratio, making it the most promising photodetector for low-noise and high-contrast light detection. This result underlines the technological relevance of the organic spacer layers in quasi-2D perovskites: beyond stabilizing the layered structure, they effectively suppress leakage pathways and minimize the dark-current background. Therefore, organic-layer engineering emerges as a powerful route to develop perovskite photodetectors with improved noise performance, enhanced signal contrast, and greater suitability for practical low-light detection applications.

Additional measurements performed on devices fabricated from crystals belonging to the same preparation batch showed stable photocurrent for more than 10^3 s of continuous illumination and reproducible switching over more than 500 light on/off cycles, without any systematic signal degradation, as detailed in figures S1 and S2 of the supporting information.

3.2. Photoresponse to monochromatic light

To further investigate the optical response of the two perovskite crystals, wavelength-dependent photocurrent measurements were performed, as reported in figure 3. For each crystal, the responsivity was evaluated as $R = I_{ph}/P_{inc}$, where I_{ph} is the photocurrent and P_{inc} is the incident optical power at each wavelength. Figure 3(a) shows the time-resolved current response of the 3D perovskite device under monochromatic illumination, with each optical pulse corresponding to a different wavelength in the 500–850 nm range. A clear and reversible photoresponse is observed throughout the investigated spectral interval, characterized by a rapid current increase upon illumination and a prompt recovery toward the dark-current level after the light is switched off. Unlike the transients recorded under supercontinuum light illumination, no additional slow current rise is observed during the initial stage of the monochromatic pulses. This difference may be related to the lower optical power density delivered under monochromatic excitation, which may be insufficient to activate the secondary light-induced process responsible for the slow component observed at high supercontinuum laser intensity. Figure 3(b) shows the corresponding responsivity as a function of wavelength for the 3D $MAPbI_3$ crystal. The device exhibits a non-monotonic spectral response, with a pronounced contribution around

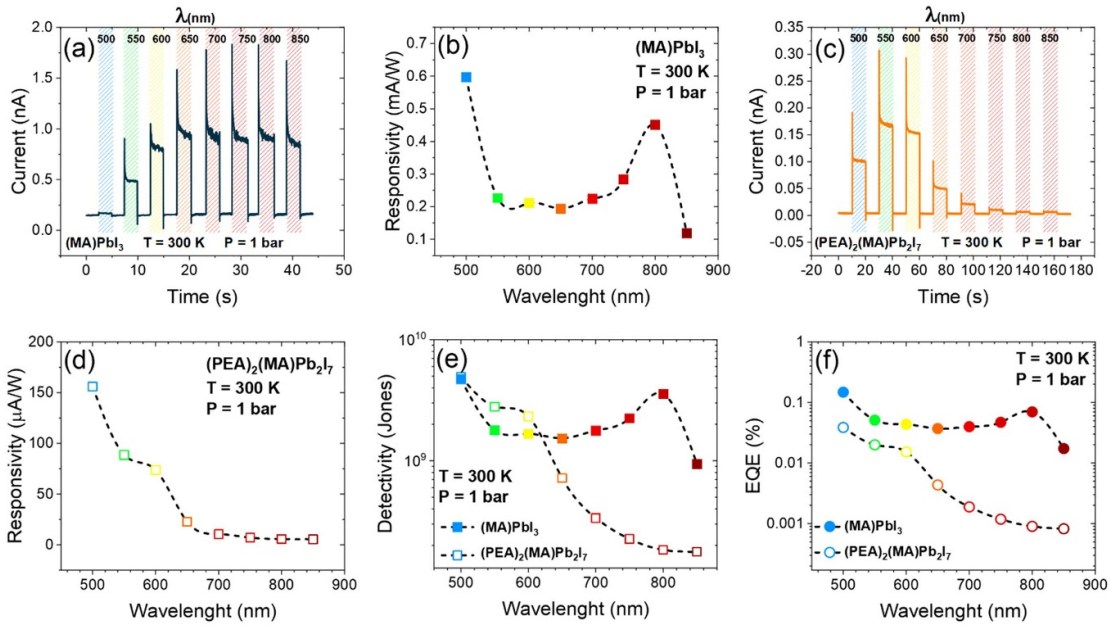

Figure 3. Response to monochromatic light. Time-dependent current measured under illumination at different wavelengths for (a) the 3D and (c) the quasi-2D perovskites. Responsivity reported as a function of the incident wavelength for (b) the 3D and (d) the quasi-2D phases. (e) Theoretical shot-noise-limited specific detectivity D^*_{shot} and (f) EQE reported for both the 3D and quasi-2D crystals as a function of wavelength. All measurements were conducted at T = 300 K and P = 1 bar.

800 nm. This wavelength corresponds to a photon energy of approximately 1.55 eV, in good agreement with the reported bandgap and the PL spectrum shown in figure 1(c) [40]. The enhanced responsivity in this spectral region can therefore be associated with direct band-edge photogeneration. A second increase is observed at shorter wavelengths, around 500 nm, corresponding to a photon energy of approximately 2.48 eV. Also this response is expected since in addition to the fundamental optical transition $E_0 \approx 1.61$ eV at the R point of the pseudocubic Brillouin zone, $MAPbI_3$ exhibits a higher-energy direct interband transition, $E_1 \approx 2.53$ eV, assigned to the M point [51]. Figure 3(c) shows the time-resolved current response of the quasi-2D perovskite device under monochromatic illumination, with each optical pulse corresponding to a wavelength between 500 and 850 nm. Also in this case, a clear and reversible response to illumination is observed across the investigated spectral range. Upon switching the light on, the current rapidly increases and subsequently approaches a quasi-steady-state value, while promptly returning to the dark-current level after illumination is removed. Sharp transient features are also observed at the switching edges, particularly at shorter wavelengths, and may be associated with rapid capacitive charging and discharging of interfacial regions as for the transient under supercontinuum illumination. Figure 3(d) reports the responsivity of the quasi-2D crystal. In this case, the response is significantly lower than that of the 3D material over the whole spectral range and becomes almost negligible above approximately 600 nm. This spectral cutoff corresponds to a photon energy of about 2.07 eV, indicating a larger bandgap than in the 3D crystal [22]. Such widening is consistent with the two-dimensional nature of the material, where the inorganic lead-iodide slabs are separated by bulky PEA organic spacer layers, leading to quantum and dielectric confinement. At shorter wavelengths, below 600 nm, the responsivity increases markedly, suggesting efficient photogeneration once the photon energy exceeds the optical gap. Figure 3(e) reports the comparison of the theoretical shot-noise-limited specific detectivity of the 3D and quasi-2D perovskite devices as a function of wavelength. At shorter wavelengths, the two devices exhibit comparable detectivity values, with the quasi-2D device even showing slightly higher D^*_{shot} around 550–600 nm owing to its strongly suppressed dark current. Above approximately 650 nm, however, the detectivity of the quasi-2D device decreases markedly as its spectral photoresponse becomes weaker, whereas the 3D device maintains values in the 10^9 Jones range over a broader spectral interval. In particular, between 750 and 800 nm, the detectivity of the quasi-2D device is approximately one order of magnitude lower than that of the 3D counterpart. This behavior is consistent with the wider bandgap and the resulting high-energy spectral selectivity of the quasi-2D perovskite. Figure 3(f) compares the external quantum efficiency, EQE, of the two crystals. The EQE was calculated from the responsivity according to $\mathrm{EQE}(\%) = Rh\frac{c}{q\lambda} \times 100$, where h is Planck's constant, c is the speed of light, q is the elementary charge, and λ is the incident wavelength. The 3D crystal shows higher EQE

values over the investigated spectral range, with maxima corresponding to the same wavelengths where the responsivity is enhanced. In contrast, the quasi-2D perovskite exhibits much lower EQE, especially at wavelengths longer than 600 nm, where the photon energy becomes insufficient to efficiently excite carriers across its wider bandgap. Overall, the comparison highlights the broader and more efficient photoresponse of the 3D crystal, while the quasi-2D perovskite shows a more spectrally selective response limited mainly to higher-energy photons.

4. Conclusions

In this work, photodetector devices based on 3D $MAPbI_3$ and quasi-2D $(PEA)_2(MA)Pb_2I_7$ single-crystals were fabricated and comparatively investigated under broadband and wavelength-resolved illumination. Both devices exhibit a clear, reversible and ohmic photoconductive response, with photocurrent increasing almost linearly with the incident optical power. However, the comparison reveals that structural dimensionality strongly affects not only the magnitude of the photoresponse, but also the intrinsic mechanisms governing charge transport, transient dynamics, dark current and noise performance.

The 3D $MAPbI_3$ device shows higher conductivity, responsivity and EQE, consistent with efficient carrier transport through its continuous inorganic Pb–I framework and broader light absorption. Nevertheless, the quasi-2D perovskite exhibits a markedly reduced dark current, lower theoretical shot-noise-limited NEP_{shot} estimate and a higher photocurrent-to-dark-current ratio, while maintaining a comparable specific detectivity. These features indicate that the organic PEA spacer layers are not merely structural elements, but play an active role in suppressing leakage pathways, confining electronic and ionic motion, and reshaping the light-induced processes occurring in the device. This is further supported by the different transient behavior: the 3D crystal shows an additional slow current rise at high optical power, compatible with light-induced ionic/electrostatic reconfiguration, whereas the quasi-2D device is dominated by faster capacitive-like charging and discharging processes.

Wavelength-dependent measurements further confirm the impact of dimensionality, showing a broader spectral response in the 3D crystal and a more selective high-energy response in the quasi-2D perovskite, consistent with the bandgap widening induced by quantum and dielectric confinement. Overall, these results demonstrate that organic-layer engineering is a powerful strategy to tune the balance between efficient photogeneration and low-noise operation in perovskite photodetectors. Continued investigation of 3D and quasi-2D perovskite architectures is therefore essential to clarify the interplay between photocarrier generation, ionic motion, interfacial charging and noise mechanisms, providing design rules for more stable, selective and high-contrast perovskite-based photodetectors.

Acknowledgment

The authors thank CeSAR-Centro Servizi di Ateneo per la Ricerca-at the Università degli Studi di Cagliari (Dr E. Podda for technical assistance on XRD). S. M. acknowledges PRIN 2022 PNRR grant P20224PJJN-Orienting.

Data availability statement

The data cannot be made publicly available upon publication because the cost of preparing, depositing and hosting the data would be prohibitive within the terms of this research project. The data that support the findings of this study are available upon reasonable request from the authors.

Stability under illumination available at: https://doi.org/10.1088/2632-959X/ae9895/data1.

Author contributions

Adolfo Mazzotti 0009-0008-9021-7874
Conceptualization (equal), Data curation (lead), Formal analysis (lead), Investigation (lead), Methodology (lead), Writing – original draft (lead)

Selene Matta
Conceptualization (equal), Data curation (equal), Formal analysis (equal), Investigation (lead), Methodology (equal), Resources (lead), Validation (equal), Writing – original draft (supporting)

Ofelia Durante 0000-0002-3539-3858
Conceptualization (supporting), Data curation (equal), Formal analysis (equal), Investigation (equal), Methodology (lead), Supervision (equal), Validation (equal), Writing – original draft (supporting)

Valeria Demontis 0000-0002-1613-4383
Conceptualization (supporting), Data curation (equal), Formal analysis (equal), Funding acquisition (supporting), Investigation (equal), Methodology (equal), Resources (equal), Supervision (equal), Validation (equal), Writing – original draft (supporting)

Sebastiano De Stefano 0009-0007-8492-0857
Data curation (equal), Formal analysis (equal), Investigation (equal), Methodology (equal), Software (equal), Validation (equal), Visualization (equal)

Andrea Sessa
Data curation (equal), Formal analysis (equal), Investigation (equal), Methodology (equal), Software (equal), Validation (equal), Visualization (equal)

Francesco De Chiara
Data curation (equal), Formal analysis (equal), Investigation (equal), Methodology (equal), Software (equal), Validation (equal), Visualization (equal)

Daniela Marongiu 0000-0001-7085-769X
Conceptualization (equal), Funding acquisition (equal), Methodology (equal), Project administration (supporting), Resources (supporting), Supervision (equal), Validation (supporting), Writing – review & editing (supporting)

Michele Saba
Conceptualization (equal), Funding acquisition (equal), Methodology (supporting), Project administration (equal), Resources (supporting), Supervision (equal), Validation (supporting), Writing – review & editing (supporting)

Giovanni Bongiovanni
Conceptualization (equal), Funding acquisition (equal), Methodology (supporting), Project administration (equal), Resources (supporting), Supervision (equal), Validation (supporting), Writing – review & editing (supporting)

Nadia Martucciello 0000-0003-1019-1587
Data curation (equal), Formal analysis (equal), Investigation (equal), Methodology (equal), Software (equal), Supervision (supporting), Validation (equal), Visualization (supporting)

Antonio Di Bartolomeo 0000-0002-3629-726X
Conceptualization (equal), Formal analysis (supporting), Funding acquisition (equal), Investigation (supporting), Methodology (equal), Project administration (lead), Resources (supporting), Supervision (lead), Validation (lead), Writing – review & editing (lead)

References

[1] Khaouani M, Sessa A, De Stefano S, Rouigueb H, Belbachir M A, Mazzotti A, Pelella A, Durante O, García-hemme E and Di Bartolomeo A 2026 Experiment and simulation in silicon PN-junction photodetectors: insights into electrical and optical transport *Physica B* **730** 418479
[2] Yang Z and Hao J 2019 Recent progress in 2D layered III–VI semiconductors and their heterostructures for optoelectronic device applications *Adv. Mater. Technol.* **4** 1900108
[3] Giubileo F *et al* 2025 Hierarchical WSe_2 nanoflowers for efficient field emission *Adv. Electron. Mater.* **11** e00490
[4] Hartner S, Schwesig D, Plümel I, Wolf D E, Lorke A and Wiggers H 2012 Electrical transport in semiconductor nanoparticle arrays: conductivity, sensing and modeling *Nanoparticles from the Gasphase NanoScience and Technology* ed A Lorke, M Winterer, R Schmechel and C Schulz (Springer) pp 231–71
[5] Pelella A, Demontis V, Sessa A, Mazzotti A, Giubileo F, Zannier V, Sorba L, Rossella F and Di Bartolomeo A 2025 Photogating in suspended InAs nanowire field effect transistors for neuromorphic applications *Adv. Electron. Mater.* **11** e00520
[6] Shao Y, Yoon J, Kim H, Lee T and Lu W 2014 Analysis of surface states in ZnO nanowire field effect transistors *Appl. Surf. Sci.* **301** 2–8
[7] Liu X, Pan Y, Yang J, Qu D, Li H, Yoo W J and Sun J 2021 High performance WSe_2 p-MOSFET with intrinsic n-channel based on back-to-back p–n junctions *Appl. Phys. Lett.* **118** 233101

[8] Viscardi L, Intonti K, Mazzotti A, Pelella A, Giubileo F, Guo Y, Sun M, Han Z V, Wang H and Di Bartolomeo A 2026 Interface-engineered $MoSe_2$ /CrOCl Complementary FETs integrating logic, memory, and neuromorphic functions *Small Struct.* **7** e202500840

[9] Furchi M M, Pospischil A, Libisch F, Burgdörfer J and Mueller T 2014 Photovoltaic effect in an electrically tunable van der Waals heterojunction *Nano Lett.* **14** 4785–91

[10] Mazzotti A, Durante O, De Stefano S, Viscardi L, Pelella A, Kharsah O, Daniel L, Sleziona S, Schleberger M and Di Bartolomeo A 2025 BP/MoS_2 van der Waals heterojunctions for self-powered photoconduction *Adv. Opt. Mater.* **13** 2500811

[11] Ali N, Attique S, Rahimi-iman A, Ali S, Akram F, Dai N and Wu H 2023 Beyond lead: progress in stable and non-toxic lower-dimensional perovskites for high-performance photodetection *Sustain. Mater. Technol.* **38** e00759

[12] Lee M M, Teuscher J, Miyasaka T, Murakami T N and Snaith H J 2012 Efficient hybrid solar cells based on meso-superstructured organometal halide perovskites *Science* **338** 643–7

[13] Demontis V *et al* 2025 Photoconduction in 2D single-crystal hybrid perovskites *Adv. Opt. Mater.* **13** 2402469

[14] Burschka J, Pellet N, Moon S-J, Humphry-baker R, Gao P, Nazeeruddin M K and Grätzel M 2013 Sequential deposition as a route to high-performance perovskite-sensitized solar cells *Nature* **499** 316–9

[15] Dong Q, Fang Y, Shao Y, Mulligan P, Qiu J, Cao L and Huang J 2015 Electron-hole diffusion lengths $>$ 175 μm in solution-grown CH_3 NH_3 PbI_3 single crystals *Science* **347** 967–70

[16] Tan Z-K *et al* 2014 Bright light-emitting diodes based on organometal halide perovskite *Nat. Nanotechnol.* **9** 687–92

[17] Dou L, Yang Y, You J, Hong Z, Chang W-H, Li G and Yang Y 2014 Solution-processed hybrid perovskite photodetectors with high detectivity *Nat. Commun.* **5** 5404

[18] Yakunin S *et al* 2015 Detection of x-ray photons by solution-processed lead halide perovskites *Nat. Photon.* **9** 444–9

[19] Wu J, Xu Y, Zhao J, Ma H, Zheng J and Zhang W 2025 Optimization of translucent perovskite solar cells based on MoO_3/metal/MoO_3 multilayer transparent electrodes *Sol. Energy* **299** 113675

[20] Ma H, Xu Y, Zhao J, Wu J, Sun L, Zheng J and Zhang W 2025 Numerical optimization of TiO_2/SnO_2 bilayer electron transport layers for enhanced perovskite solar cell performance *Discov. Nano* **20** 161

[21] Durante O *et al* 2025 Trap-assisted transport and neuromorphic plasticity in lead-free 2D perovskites PEA_2 SnI_4 *Adv. Funct. Mater.* **36** e26339

[22] Kim H, Choi M-J, Suh J M, Han J S, Kim S G, Le Q V, Kim S Y and Jang H W 2020 Quasi-2D halide perovskites for resistive switching devices with ON/OFF ratios above 109 *NPG Asia Mater.* **12** 21

[23] Leung T L, Ahmad I, Syed A A, Ng A M C, Popović J and Djurišić A B 2022 Stability of 2D and quasi-2D perovskite materials and devices *Commun. Mater.* **3** 63

[24] Blancon J-C *et al* 2018 Scaling law for excitons in 2D perovskite quantum wells *Nat. Commun.* **9** 2254

[25] Wang J, Li J, Lan S, Fang C, Shen H, Xiong Q and Li D 2019 Controllable growth of centimeter-sized 2D perovskite heterostructures for highly narrow dual-band photodetectors *ACS Nano* **13** 5473–84

[26] Lin C-C *et al* 2022 Direct investigation of the reorientational dynamics of A-site cations in 2D organic-inorganic hybrid perovskite by solid-state NMR *Nat. Commun.* **13** 1513

[27] Matta S *et al* 2025 One-pot growth of 2D/3D hybrid perovskite vertical heterostructures *ACS Mater. Lett.* **7** 3908–15

[28] Oku T, Ohishi Y and Ueoka N 2018 Highly (100)-oriented CH_3 NH_3 PbI_3 (Cl) perovskite solar cells prepared with NH_4 Cl using an air blow method *RSC Adv.* **8** 10389–95

[29] Ishii A, Noto M, Nakamura D, Matsumura S and Suzuki K 2025 Evaluation of internal quantum efficiency in $MAPbI_3$ single crystals via omnidirectional photoluminescence spectroscopy *Chem. Lett.* **54** upaf153

[30] Yamada Y, Yamada T, Phuong L Q, Maruyama N, Nishimura H, Wakamiya A, Murata Y and Kanemitsu Y 2015 Dynamic optical properties of CH_3 NH_3 PbI_3 single crystals as revealed by one- and two-photon excited photoluminescence measurements *J. Am. Chem. Soc.* **137** 10456–9

[31] Lekina Y, Dintakurti S S H, Febriansyah B, Bradley D, Yan J, Shi X, England J, White T, Hanna J V and Shen Z X 2021 The effect of organic cation dynamics on the optical properties in $(PEA)_2$ (MA)$[Pb_2$ $I_7]$ perovskite dimorphs *J. Mater. Chem. C* **9** 17050–60

[32] Zhou H, Feng Q, Sun C, Li Y, Tao W, Tang W, Li L, Shi E, Nan G and Zhu H 2024 Robust excitonic light emission in 2D tin halide perovskites by weak excited state polaronic effect *Nat. Commun.* **15** 8541

[33] Mazzotti A *et al* 2026 Defect-tuned conduction in ultrathin $MoTe_2$ field-effect transistors *J. Mater. Chem. C* **14** 9773–87

[34] Xue H, Chen Z, Tao S and Brocks G 2024 Defects in halide perovskites: does it help to switch from 3D-2D? *ACS Energy Lett.* **9** 2343–50

[35] Gonzales C, Bou A, Guerrero A and Bisquert J 2024 Capacitive and inductive characteristics of volatile perovskite resistive switching devices with analog memory *J. Phys. Chem. Lett.* **15** 6496–503

[36] Hu J, Gottesman R, Gouda L, Kama A, Priel M, Tirosh S, Bisquert J and Zaban A 2017 Photovoltage behavior in perovskite solar cells under light-soaking showing photoinduced interfacial changes *ACS Energy Lett.* **2** 950–6

[37] Calado P, Telford A M, Bryant D, Li X, Nelson J, O'regan B C and Barnes P R F 2016 Evidence for ion migration in hybrid perovskite solar cells with minimal hysteresis *Nat. Commun.* **7** 13831

[38] Azpiroz J M, Mosconi E, Bisquert J and De Angelis F 2015 Defect migration in methylammonium lead iodide and its role in perovskite solar cell operation *Energy Environ. Sci.* **8** 2118–27

[39] Thiesbrummel J *et al* 2024 Ion-induced field screening as a dominant factor in perovskite solar cell operational stability *Nat. Energy* **9** 664–76

[40] Zhao Y-C, Zhou W-K, Zhou X, Liu K-H, Yu D-P and Zhao Q 2016 Quantification of light-enhanced ionic transport in lead iodide perovskite thin films and its solar cell applications *Light Sci. Appl.* **6** e16243

[41] Sessa A *et al* 2026 Synaptic behavior in $SnSe_2$ field-effect transistors induced by surface oxide and trap dynamics *Adv. Electron. Mater.* **12** e00734

[42] Intonti K *et al* 2026 Ambipolar to anti-ambipolar light-induced transition in WSe_2 -based FETs *Mater. Horiz.* **13** 2583–94

[43] Saidaminov M I, Adinolfi V, Comin R, Abdelhady A L, Peng W, Dursun I, Yuan M, Hoogland S, Sargent E H and Bakr O M 2015 Planar-integrated single-crystalline perovskite photodetectors *Nat. Commun.* **6** 8724

[44] Li C, Li J, Li Z, Zhang H, Dang Y and Kong F 2021 High-performance photodetectors based on nanostructured perovskites *Nanomaterials* **11** 1038

[45] Bao C, Yang J, Bai S, Xu W, Yan Z, Xu Q, Liu J, Zhang W and Gao F 2018 High performance and stable all-inorganic metal halide perovskite-based photodetectors for optical communication applications *Adv. Mater.* **30** 1803422

[46] Liu Y, Zheng X, Fang Y, Zhou Y, Ni Z, Xiao X, Chen S and Huang J 2021 Ligand assisted growth of perovskite single crystals with low defect density *Nat. Commun.* **12** 1686

[47] Lian Z, Yan Q, Lv Q, Wang Y, Liu L, Zhang L, Pan S, Li Q, Wang L and Sun J-L 2015 High-performance planar-type photodetector on (100) facet of $MAPbI_3$ single crystal *Sci. Rep.* **5** 16563
[48] Ji L, Hsu H-Y, Lee J C, Bard A J and Yu E T 2018 High-performance photodetectors based on solution-processed epitaxial grown hybrid halide perovskites *Nano Lett.* **18** 994–1000
[49] Perumal Veeramalai C, Yang S, Zhi R, Sulaman M, Saleem M I, Cui Y, Tang Y, Jiang Y, Tang L and Zou B 2020 Solution-processed, self-powered broadband CH_3 NH_3 PbI_3 photodetectors driven by asymmetric electrodes *Adv. Opt. Mater.* **8** 2000215
[50] Ollearo R, Wang J, Dyson M J, Weijtens C H L, Fattori M, van Gorkom B T, van Breemen A J J M, Meskers S C J, Janssen R A J and Gelinck G H 2021 Ultralow dark current in near-infrared perovskite photodiodes by reducing charge injection and interfacial charge generation *Nat. Commun.* **12** 7277
[51] Shirayama M *et al* 2016 Optical transitions in hybrid perovskite solar cells: ellipsometry, density functional theory, and quantum efficiency analyses for CH_3 NH_3 PbI_3 *Phys. Rev. Appl.* **5** 014012